

A Global View on the Wind Sea and Swell Climate and Variability from ERA-40

ALVARO SEMEDO

Department of Earth Sciences, Uppsala University, Uppsala, Sweden, and Escola Naval, CINAV, Lisbon, Portugal

KAY SUŠELJ

Jet Propulsion Laboratory, California Institute of Technology, Pasadena, California

ANNA RUTGERSSON

Department of Earth Sciences, Uppsala University, Uppsala, Sweden

ANDREAS STERL

Royal Netherlands Meteorological Institute (KNMI), De Bilt, Netherlands

(Manuscript received 9 March 2010, in final form 13 October 2010)

ABSTRACT

In this paper a detailed global climatology of wind-sea and swell parameters, based on the 45-yr European Centre for Medium-Range Weather Forecasts Re-Analysis (ERA-40) wave reanalysis is presented. The spatial pattern of the swell dominance of the earth's oceans, in terms of the wave field energy balance and wave field characteristics, is also investigated. Statistical analysis shows that the global ocean is strongly dominated by swell waves. The interannual variability of the wind-sea and swell significant wave heights, and how they are related to the resultant significant wave height, is analyzed over the Pacific, Atlantic, and Indian Oceans. The leading modes of variability of wind sea and swell demonstrate noticeable differences, particularly in the Pacific and Atlantic Oceans. During the Northern Hemisphere winter, a strong north-south swell propagation pattern is observed in the Atlantic Ocean. Statistically significant secular increases in the wind-sea and swell significant wave heights are found in the North Pacific and North Atlantic Oceans.

1. Introduction

The ocean wave spectrum is dominated by wind waves accounting for more than half of the energy carried by all waves at the surface, surpassing the contribution of tides, tsunamis, coastal surges, and others. There are two types of wind waves (henceforth simply called waves) at the ocean surface. During the generation and growing processes, they are designated as wind sea. As waves propagate away from their generation area, or when their phase speed overcomes the overlying wind speed, they are called swell. Swell waves are known to travel long distances across the globe (Barber and Ursell 1948; Munk et al. 1963; Snodgrass

et al. 1966). Wind seas are generated locally and are strongly coupled to the local wind field; swells are generated remotely and are not directly coupled to the local wind field.

The generation and growing processes of wind seas have been the main focus in the development of wave models for forecasting purposes. Since swell waves carry most of the wave energy at the ocean surface, the main concern has been its impact on offshore and coastal infrastructures. Recently, there has been a renewed interest in the study of swell, from propagation and attenuation (Alves 2006; WISE Group 2007; Ardhuin et al. 2009) to the swell impact on the marine atmospheric boundary layer (MABL) (Sullivan et al. 2008; Högström et al. 2009). It has been shown that swell decay rates are related to a reverse momentum flux process (Donelan et al. 1997; Grachev and Fairall 2001), occurring as swell performs work on the overlying atmosphere (Semedo et al. 2009).

Corresponding author address: Alvaro Semedo, Department of Earth Sciences, Uppsala University, Villavägen 16, SE-752 36 Uppsala, Sweden.
E-mail: alvaro.semedo@met.uu.se

Several global-scale wave climatology studies have been published in recent years: Barstow (1996) and Young (1999), using satellite altimetry and model hindcasts, and Sterl and Caires (2005), using only model hindcast reanalysis. These studies, like previous wave climatologies and atlases, focused on the most important wave parameters: significant wave height (SWH) and mean wave period (MWP). However, these two parameters give only a limited description of the wave field characteristics, as two fields with the same SWH and MWP may still be very different in detail: a mixed sea state of wind sea and swell may have the same SWH and MWP as a slightly higher wind sea without swell. To distinguish such conditions, additional information about SWH, MWP, and their propagating directions [mean wave direction (MWD)] is needed for wind sea and swell separately. A detailed qualitative description of the ocean wave field is important for many scientific and practical reasons, such as the design of offshore and coastal structures or the study of the swell impact on the MABL. The separate analysis of wind-sea and swell parameters also provides a better understanding of the mechanisms of climate variability in the wave field, since wind sea reflects variations in the local wind only, while swell variability reflects wind changes over a larger domain (Hogben 1995; Bauer et al. 1997).

Chen et al. (2002), Gulev et al. (2003), and Gulev and Grigorieva (2006) (hereafter CCEV02, GGSW03, and GG06, respectively) complemented existing wave climatologies by highlighting the differences between the two wave regimes. CCEV02 used 10 yr of combined satellite altimetry and wave model results to assess the global geographic distribution and frequency of occurrence of wind sea- and swell-dominated wave fields. In view of the World Meteorological Organization recommendations, which states a minimum of 30 yr for climate studies, the length of the data used by CCEV02 can be seen as short. GGSW03 presented a global distribution of SWH, and wind-sea and swell heights and periods from more than 40 yr of visual wave observations from voluntary observing ships (VOS). The focus of GG06 was on the winter interannual and long-term variability of wind-sea and swell heights, also from VOS, in the North Atlantic (NA) and North Pacific (NP). Although complementary, these studies used different wind sea–swell classification schemes: CCEV02 used the wind–wave relation for fully developed seas from the Wave Model (WAM) (WAMDI Group 1988; Komen et al. 1994), while GGSW03 and GG06 used the visual observers' subjective criteria. One of the most important questions concerning the reliability of the VOS wave data is the uncertainty of the separation between wind-sea and swell heights, which depends on the human observers' judgment and experience. Despite these

limitations, VOS wave data have been proved to be very useful (Hogben et al. 1986) and successfully used in compiling global and regional wave climate and statistics (Korevaar 1990; Gulev and Hasse 1998, 1999; Gulev and Grigorieva 2004).

Spectral partitioning is the best way to isolate wind-sea and swell characteristics (Gerling 1992; Hanson and Phillips 2001). A global and long enough spectral description of the wave field is only available from wave model hindcasts, such as the 45-yr European Centre for Medium-Range Weather Forecasts (ECMWF) Re-Analysis (ERA-40). This study presents a detailed global climatology, based on ERA-40, of wind-sea and swell characteristics, complementing and validating previous studies. The global distribution of wind-sea and swell SWH and MWD parameters, available from the ERA-40 archive, is presented here for the first time. The interannual variability and long-term trends of SWH and its wind-sea and swell components in the Northern Hemisphere (NH) are analyzed.

It is known that in ERA-40, low wave heights tend to be overestimated and high wave heights tend to be underestimated (Sterl and Caires 2005), and that high wind speeds are slightly underestimated (Caires and Sterl 2003). The correct modeling of taller waves under extreme condition is still an open question (Cavaleri 2009). The problem of quantitatively understanding to which extend the long-term wave height variability is driven by winds or by the model settings remains, since for large scales most models give similar results under the same wind forcing. We chose modeled wave data for our study because presently these are the only type of data for which global wave spectra, as well wind-sea and swell parameters, are available. The ERA-40 wave reanalysis was chosen because of its length and quality (Caires et al. 2004).

Sterl and Caires (2005) produced a statistically corrected dataset (C-ERA-40) of SWH. They did not correct the wind-sea and swell SWH or MWP, since that would have implied correcting the modeled wave spectra themselves. Because of the lack of observed spectral data, this was not possible. We are therefore left with the only choice of using "uncorrected" wind-sea and swell parameters (see section 2). For consistency we also used the uncorrected SWH data.

Section 2 describes ERA-40. The climatologies of wind-sea and swell characteristics are presented in section 3. Section 4 presents the interannual variability of wind-sea and swell waves, as well as their correlation with large-scale atmospheric circulation patterns. The long-term variability of wind-sea and swell heights and how they combine in the overall SWH variability are presented in section 5. The concluding remarks and suggestions for further research are presented in section 6.

2. Data and methods of analysis

a. ERA-40

A reanalysis aim is to overcome the inhomogeneities related to model and data assimilation changes. The best available model and data assimilation scheme that do not change in time are used to repeat the analysis procedure; therefore, a reanalysis yields a complete dataset that is as temporally homogeneous as possible. Unfortunately, inhomogeneities due to uneven data coverage and changes in observation systems still remain (Uppala 1997; Sterl 2004). For waves the biggest inhomogeneities are related to the assimilation of altimeter data in ERA-40 (see below).

ERA-40 is a reanalysis of meteorological observations from September 1957 to August 2002 (45 yr), produced by the ECMWF (Uppala et al. 2005). The dataset consists of 6-hourly global fields with a $1.5^\circ \times 1.5^\circ$ grid resolution. Besides atmospheric variables, it also includes wave parameters. ERA-40 was produced using the ECMWF Integrated Forecasting System, a two-way coupled atmosphere–wave model system and a three-dimensional variational data assimilation (3DVAR) scheme. Observations of ocean wind speeds from VOS, buoys, and satellite scatterometer were assimilated in the reanalysis process. Since 1991 satellite altimeter SWHs were also assimilated. The wave model used in the coupled system is the third-generation WAM. The ERA-40 wave data, mostly due to changes in the satellite products assimilated in the process, are not fully homogeneous in time. Four different periods are clearly identified by Sterl and Caires (2005). In one of these periods (from December 1991 to May 1993) erroneous remote sensing data were assimilated, giving rise to corrupted wave model output. We choose not to use data from this period in our analysis. Additional details about the ERA-40 wave reanalysis are given by Sterl and Caires (2005), Caires and Sterl (2005), and Caires et al. (2005). Details about comparisons between ERA-40 and similar wave reanalysis products, in which the ERA-40 proved to be of superior quality, are given by Caires et al. (2004).

b. Wave parameters

The WAM output is the two-dimensional (2D) wave energy spectrum $F(f, \theta)$, obtained at each grid point by integrating the wave energy balance equation (Komen et al. 1994). The $F(f, \theta)$ spectrum describes how the mean sea surface elevation variance is distributed as a function of frequency (f) and propagation direction (θ). From $F(f, \theta)$ several integrated wave parameters can be obtained. Besides wave parameters, ERA-40 10-m wind speed (U_{10}) and direction (φ) are also used.

The SWH concept, originally defined by Munk (1944) as the mean of the highest one-third of all individual waves in a record, is statistically related to the mean variance of the sea surface elevation (the zeroth moment): $\text{SWH} = H_s = 4.04\sqrt{m_0}$, where

$$m_0 = \iint f^0 F(f, \theta) df d\theta \quad (1)$$

is the zeroth moment. The characteristic MWP used in this study is $T_{m_{-1.0}} = m_{-1}/m_0$, where

$$m_{-1} = \iint f^{-1} F(f, \theta) df d\theta. \quad (2)$$

The MWD is defined as $\theta_m = \text{atan}(\text{SF}/\text{CF})$, where

$$\text{SF} = \iint \sin(\theta) F(f, \theta) df d\theta \quad \text{and} \quad (3)$$

$$\text{CF} = \iint \cos(\theta) F(f, \theta) df d\theta. \quad (4)$$

The SWH, MWP, and MWD of wind sea (H_s^w, T_m^w, θ_m^w) and swell (H_s^s, T_m^s, θ_m^s) are computed by separating the 2D energy spectrum into wind-sea and swell components. In WAM the separation frequency is defined as the frequency corresponding to the wave phase speed \hat{c} , where $\hat{c}/u_* \cos(\theta - \varphi) = 1.2 \times 28$ (Bidlot 2001) and u_* is the friction velocity. The factor 28 corresponds to the peak phase speed $c_p = 28u_*$ from the Pierson–Moskowitz spectrum and 1.2 is a tuning parameter. The high- and low-frequency parts of the partitioned spectrum correspond to the wind-sea and swell components, respectively. The wind-sea and the swell parameters are computed by integrating over the respective spectral parts.

3. Climatology of the global wave field characteristics

The 6-hourly gridded values of wind and wave parameters were processed to seasonal means, organized as December–February (DJF), March–May (MAM), June–August (JJA), and September–November (SON). Here we focus only on the extreme seasons DJF and JJA.

a. Wind-sea and swell significant wave heights

Figure 1 displays the seasonal maps for the DJF and JJA mean U_{10} global fields. The arrows represent the climatological seasonal means of φ , and their magnitudes are scaled with the background U_{10} fields. The mean φ (as with $\theta_m, \theta_m^s, \text{ and } \theta_m^w$) was obtained by averaging the x and y components of the wind separately. The DJF and JJA U_{10} fields are characterized by high values in the extratropical areas and low values in the tropics. The U_{10} seasonal

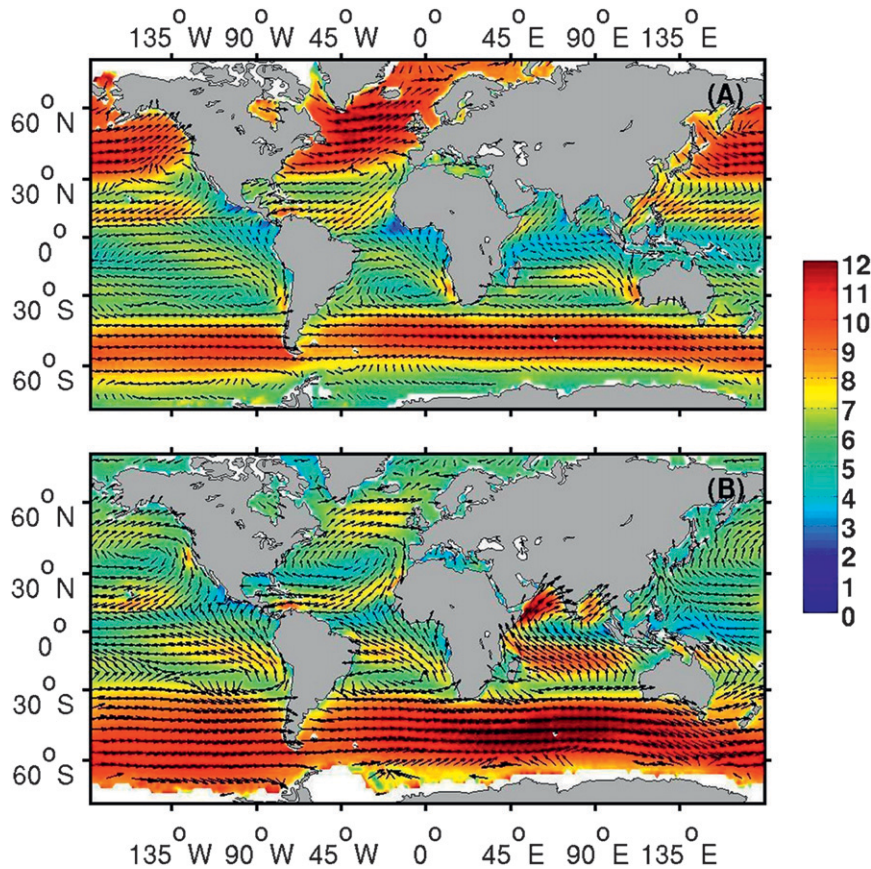


FIG. 1. Seasonal averages of U_{10} (m s^{-1}) and φ ($^{\circ}$) for (a) DJF and (b) JJA. The arrows are scaled with the background field (see text).

variability in the NH, particularly in the NA, is greater than in the Southern Hemisphere (SH). The Southern Ocean (SO) U_{10} mean maximum, in both seasons, is located in its Indian sector. The U_{10} features in the trade winds shows little variability between DJF and JJA. Some regional U_{10} features have a potential impact on the local to global wave field. Examples are the California, Namibia, and Somalia low-level coastal jets, peaking in the respective hemisphere summer, and the Indian Ocean (IO) monsoon.

The seasonal maps of H_s , H_s^s , and H_s^w are shown in Figs. 2 and 3. The arrows represent the climatological seasonal means of θ_m , θ_m^s , and θ_m^w , and their magnitudes are scaled with the background fields. The highest seasonal mean H_s conditions are found in the extratropical areas in both hemispheres. The H_s seasonal mean maxima in the SH are located in the SO Indian sector. The H_s mean maxima in JJA and DJF, in the NA and NP, reflect the higher seasonality of H_s in the NH. The NP H_s maximum in JJA is located off the coast of the United States, because of the summer coastal U_{10} enhancement. The highest mean H_s^s values are found during the respective hemisphere winter, in the extratropical areas, but also along the trade winds. The variability of the H_s^s maxima

between DJF and JJA is higher in the NA than in the NP, because of the higher predominance of swell in the Pacific Ocean (PO, see below). In the SO the highest seasonal mean H_s^s values are also found along the Indian sector. The swell propagation features away from the wave generation areas are very visible and will be discussed further.

The highest mean H_s^w values are also found during the hemisphere winter in the extratropical areas. The lowest mean H_s^w values (close to zero) in both seasons are found in the low latitudes. In the SH the H_s^w seasonal mean maxima are located in the SO Indian sector in both seasons. In JJA, in the NH, the highest seasonal mean H_s^w values are found along the trade winds. In DJF, in the SO Indian sector, the H_s^w maximum is almost as high as in the NP in the same season. Several local H_s^w enhancement areas occur along local U_{10} features (e.g., Somali low-level coastal jet and the Indian monsoon).

General features of the H_s^w and U_{10} fields are the collocation of their seasonal mean maxima and the high alignment between φ and θ_m^w , reflecting the coupling between both fields. This is not the case for φ and θ_m^s , since swell waves are independent of the local wind. In the extratropical areas, wind-sea and swell waves are more or

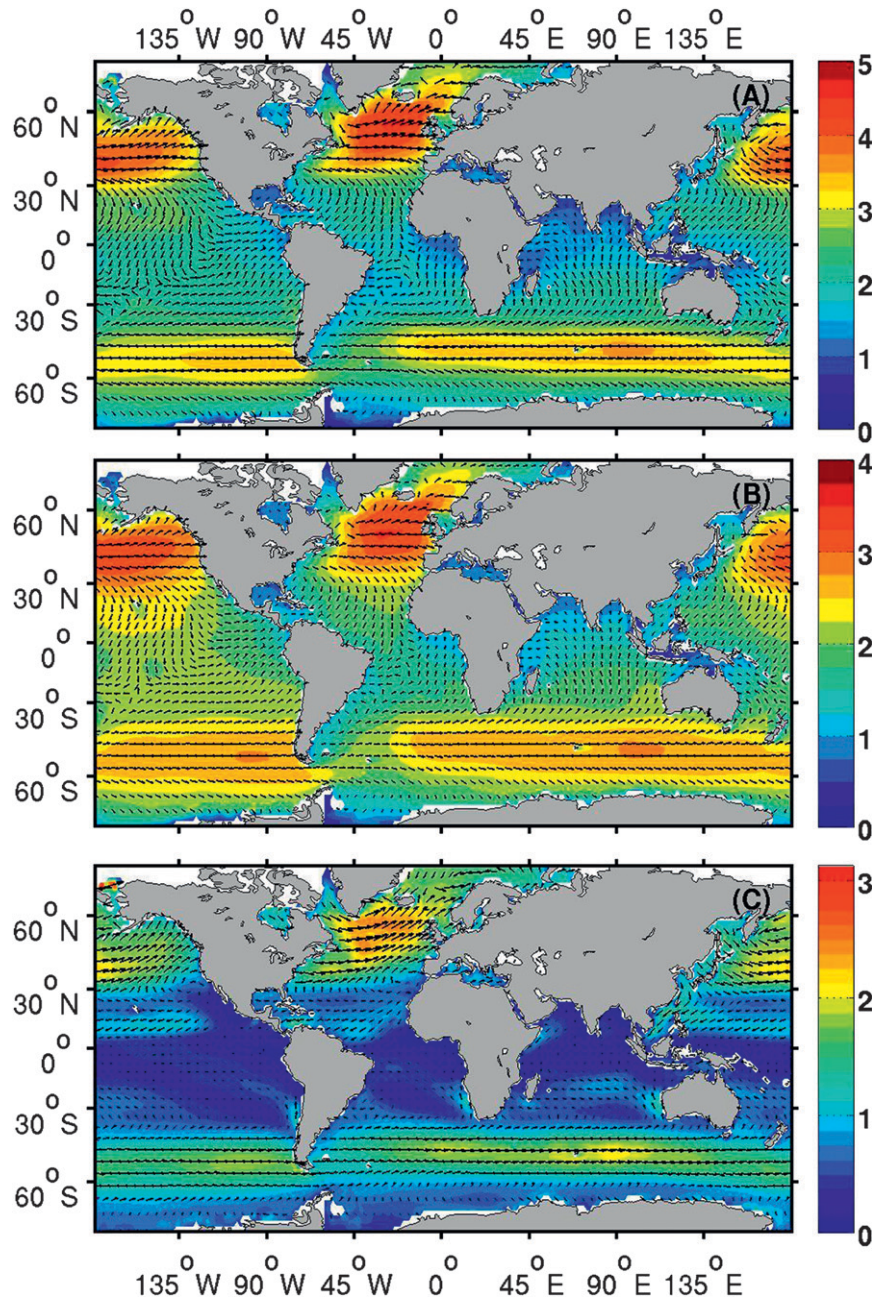


FIG. 2. Seasonal averages for DJF of (a) H_s (m) and θ_m ($^\circ$), (b) H_s^s (m) and θ_m^s ($^\circ$), and (c) H_s^w (m) and θ_m^w ($^\circ$). The arrows are scaled with the background fields. The color scales vary between the panels (see text).

less aligned with the wind direction. Elsewhere, the angle between φ and θ_m^w can still be very high, such as in the tropical and subtropical latitudes or close to 180° , as in the Pacific coast of Central America and in the Arabian Sea in DJF.

The swell propagation patterns in the PO are more complicated, since they are affected by waves generated in both hemispheres. During DJF the “swell front” (Young

1999) is very well defined in Figs. 2a and 2b. Extending from New Zealand to Central America, it marks the boundary between the domains of dominance of swell from each of the hemispheres (Young 1999). North of the front, the θ_m^s is from the north, consistent with swell that propagates equatorward a way from the NP extratropical storm area; south of the front, θ_m^s is from the south, consistent with swell originating along the SO extratropical storms.

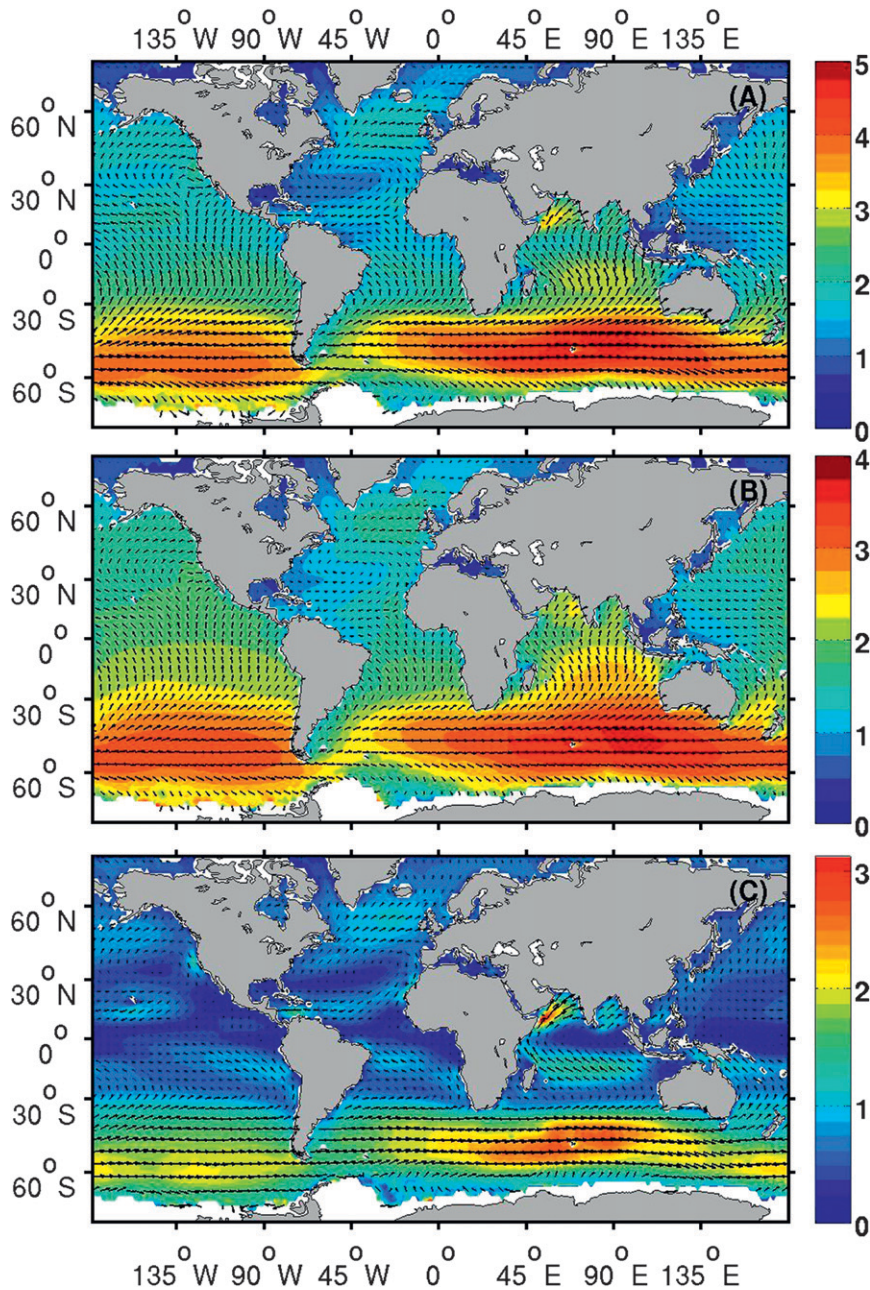


FIG. 3. As in Fig. 2, but for JJA.

During MAM (not shown), the front moves northward because of the strengthening of swell waves generated along the SO extratropical area. In JJA (Fig. 3b), the eastern PO H_s^2 field is dominated by SO swell. In SON (not shown), the front builds up again; however, now along the equator, as the extratropical storms in the NP get more intense. Although less prominent than in the PO, a swell front can also be identified in the Atlantic Ocean (AO). Young (1999) mentioned that this feature does not migrate north of the equator. In our

results, the swell front in the Atlantic is present in all seasons, although confined to a latitude band from 15°S (DJF) to 15°N (JJA). The swell fronts in the PO and AO are better defined here than in Young (1999), since we separate the wind-sea and swell components of the wave field.

Besides wave reanalysis, the only global wave dataset that separates wind-sea and swell parameters are visual wave estimates from VOS. Although using a different separation criterion (see the introduction), GGSW03

concluded that the wind sea and swell separation in WAM and in VOS can be assumed as “equivalent,” so that a comparison is possible. GGSW03 made several tests and comparisons between VOS and ERA-15, a previous ECMWF reanalysis project (Sterl et al. 1998). We assume that the criteria that allowed the comparison between VOS wave parameters and ERA-15 in GGSW03 are also valid for ERA-40.

The climatology of VOS wave parameters in GGSW03 covers the period 1958–97. Annual mean fields of H_s^s and H_s^w from ERA-40 were reprocessed for the same period (not shown). A rough visual comparison between the VOS wind-sea and swell heights and the H_s^s and H_s^w annual mean fields revealed several differences. In the NH extratropical storm areas, the VOS mean swell heights are higher (0.4–0.6 m) than those H_s^s from ERA-40. In the tropics, the ERA-40 H_s^s annual means are generally higher than those from VOS by 0.1–0.3 m and by up to 0.4 m in the SO extratropical storm tracks. The ERA-40 H_s^w annual means in the NH extratropics and subtropical areas are similar to the wind-sea heights from VOS. In the tropics, the annual mean wind-sea heights from VOS estimates are generally higher (0.25–0.5 m) and considerably lower in the SO storm belt. While the VOS wind-sea mean heights there range from 1.5 to 1.75 m, the ERA-40 H_s^w annual mean maxima vary from 1.5 m in the Atlantic sector to 2.8 m in the Indian sector. In the VOS wave height estimates, the highest sampling biases are observed in the SO, where wave heights can be underestimated by 1–1.5 m because of poor sampling (GGSW03, their Fig. 12). The impact of regional wind features is not present in the VOS wind sea heights, with the exception of the Somali coastal jet. Moreover, the spatial patterns of the wind-sea and swell heights from VOS appear to be more related to each other than the H_s^s and H_s^w annual mean fields from ERA-40, where the north–south swell propagation patterns seem to be better represented.

b. Energy content of the wind-sea and swell fields

It is clear from the H_s^s and H_s^w seasonal fields (Figs. 2 and 3) that swell SWH are always higher than the wind-sea SWH. From a statistical point of view, this means that swell dominates the wave spectra, that is, $m_0^s > m_0^w$, where m_0^s and m_0^w are the swell and wind-sea zeroth moments, respectively. From an energy density perspective, this also means that the energy content of the swell part of the wave field spectra is higher than the wind-sea part, that is, $E^s = \rho g m_0^s > E^w = \rho g m_0^w$, where ρ is the water density, g is the gravitational acceleration, and E^s and E^w are the energy densities per unit area (J m^{-2}) from swell and wind sea, respectively. This characteristic of the global wave field has been known through empirical evidence or from extrapolation of buoy measurements. Nevertheless, the

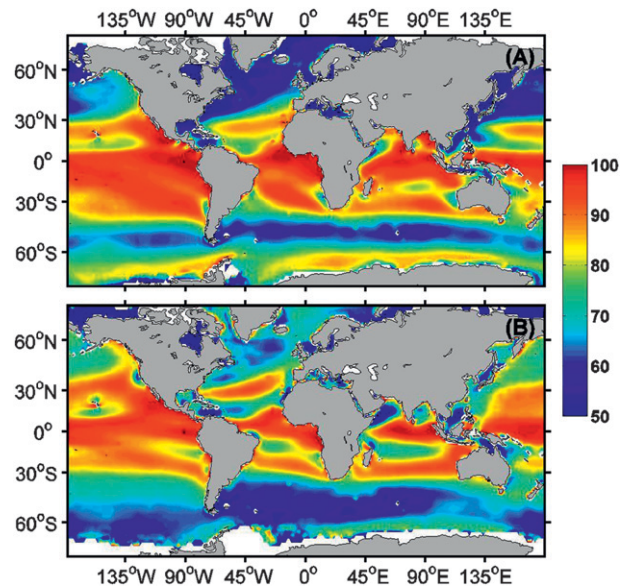


FIG. 4. Global distributions of swell energy weight (W_s ; dimensionless) for (a) DJF and (b) JJA.

global characterization of this dominance is only possible from a spectral description of the global wave field.

Figure 4 displays the DJF and JJA global spatial distribution of the swell energy proportion to the total wave energy at the surface, $W_s = E^s/E$. Clearly, swell carries most of the wave energy with W_s being higher than 65% almost everywhere, even along the extratropical areas during the respective hemisphere winter. In the NH, W_s is lower along the eastern continental coasts (<50%) but increases toward the western coasts of North America and Europe, reflecting the swell propagation effect along and away from the extratropical storm tracks.

In JJA, W_s is consistently higher than 75% in the NP, whereas in the central NA, it is only about 60%. The relatively constant lowest values of W_s in the SO storm belt (55% in DJF to 65% in JJA) reflect the low seasonality of the wave climate there. The W_s values close to the equator are always higher than 95% and close to 100% at the western continental coasts. The signature of locally enhanced U_{10} features is seen off the coasts of California and Morocco (JJA), off the coast of Somalia (both seasons), off the coast of Namibia and Chile (DJF), and during the Indian monsoon (JJA). The physical picture behind these patterns is that waves are produced in areas of high wind speeds; after a short time, waves lose direct contact with the wind and become swell, which leaves the wave-generation area and fills the whole ocean.

The wave energy fluxes (wave power per unit crest length, kW m^{-1}) were computed according to Holthuijsen (2007), where

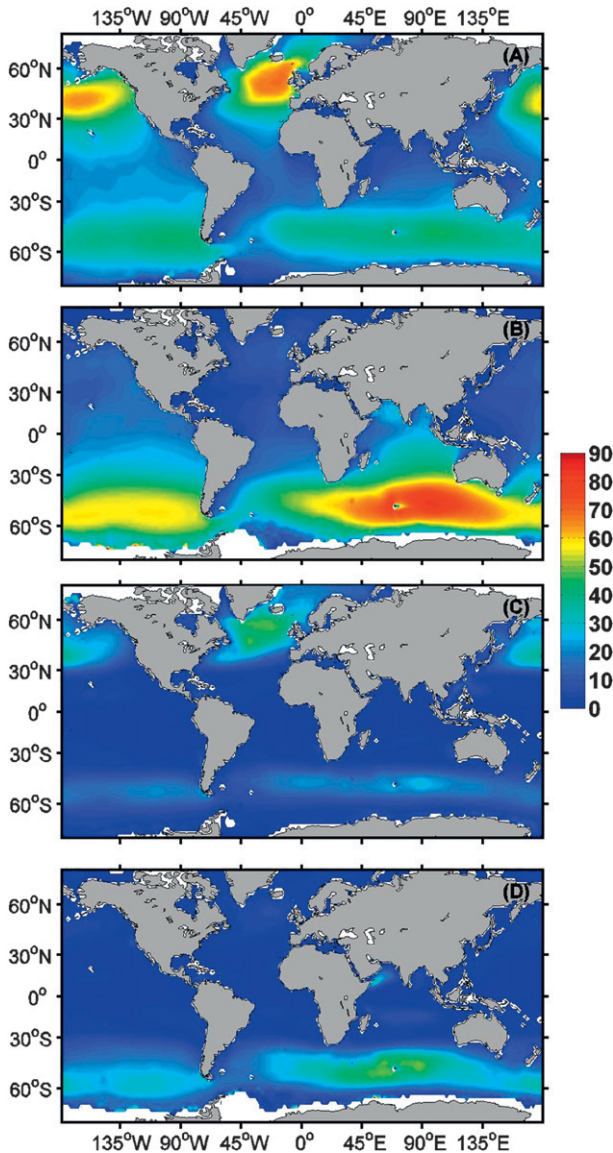


FIG. 5. Seasonal averages of E_f^s (kW m^{-1}) for (a) DJF and (b) JJA, and E_f^w (kW m^{-1}) for (c) DJF and (d) JJA.

$$E_f^w = c_g E^w = \frac{\rho g^2}{64\pi} T_m^w (H_s^w)^2 \quad \text{and} \quad (5)$$

$$E_f^s = c_g E^s = \frac{\rho g^2}{64\pi} T_m^s (H_s^s)^2 \quad (6)$$

are the wind-sea and swell energy fluxes, respectively, and c_g is the group velocity. Figure 5 displays the seasonal maps of the DJF and JJA E_f^s and E_f^w global mean fields. With the exception of the extratropical areas in both hemispheres, and predominantly in the respective winter, E_f^w is relatively low everywhere. The E_f^s mean maxima are concentrated in the extratropical areas; however, the swell propagation patterns contribute to a wider area of high

E_f^s , eventually reaching the west coasts of the continental masses but also South Africa, south Australia, and the Tasman Sea. The separate description of the wind-sea and swell wave power content is important for future operational wave energy power plants. Most of the wave energy converters will have to be optimally tuned to be in resonance with swell, because these waves carry most of the energy and are more regular than wind sea. The E_f^s maxima in both winter hemispheres occur always in deep ocean, far away from the coastal areas. Exceptions to this rule are the British Isles, the north coast of the Iberian Peninsula, the west and south coasts of Australia, and the south coast of New Zealand.

c. Swell probability

The wave field is dominated by wind sea (swell) if the wave age c_p/U_{10} is smaller (larger) than 1.2 (Pierson and Moskowitz 1964; Smith et al. 1992), where c_p is the peak wave phase speed. Given the complexity of the wave field, the classification of any true sea state into either swell- or wind-sea-dominated can be seen as simplistic, but it gives a statistically meaningful description.

To quantify the frequency of occurrence of swell-dominated wave fields, we follow a similar approach as CCEV02 and compute a probability index for each grid point for each season:

$$P_s = \frac{N_s}{N}, \quad (7)$$

where $P_s = P(c_p/U_{10} > 1.2)$ is the probability of having a swell-dominated wave field, N_s is the number of swell-dominated events, and $N = N_{ws} + N_s$, where N_{ws} is the number of wind-sea-dominated events.

The DJF and JJA global spatial distributions of P_s are shown in Fig. 6. The probabilities vary geographically and seasonally, but it is clear that a systematic swell dominance exists in the World Ocean, with P_s being higher than 75% almost everywhere. Not surprisingly, the spatial distribution of P_s is similar to the distribution of W_s (Fig. 4). At low latitudes, the wave field is practically swell dominated 100% of the time. CCEV02 called these highly swell-dominated areas “swell pools.” The trade winds signature in the P_s distribution is noticeable in DJF and JJA in both hemispheres. Some regional U_{10} enhancement features are also noticeable, with a decrease in P_s ; the low-level coastal jets in California, Peru, Namibia and Somalia, and the Indian monsoon.

Since no information about c_p was available in their remote sensing data, CCEV02 used the wind-wave relation for fully developed seas from WAM as separation criterion. Despite this, our results are in line with their findings. The seasonal variations and local details are

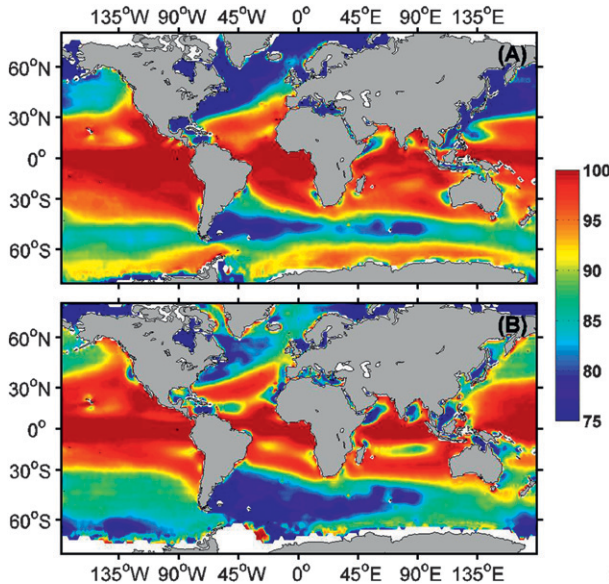


FIG. 6. As in Fig. 4, but of swell probability (P_s).

nevertheless more distinguishable here, probably because of the wind sea–swell separation criterion being more appropriate, and/or to a longer dataset. The seasonal variations of the swell probability (geographical, hemispherical, and global, obtained by averaging P_s) are presented in Table 1. The PO, AO, and IO include their respective SO sectors. The swell occurrence undergoes an opposite annual cycle in the two hemispheres and is anti-correlated with the annual wind speed: in the NH, P_s reaches a maximum in JJA and a minimum in DJF, and the SH has the opposite cycle. The globally averaged P_s shows very little seasonality because of the cancellation effect of the opposite hemispherical cycles. Our swell probability numbers are very similar to those of CCEV02: slightly lower in the NH and slightly higher in the SH, though. The IO has a distinctive swell regime, since it has only one extratropical storm area. Moreover, in the North Indian Ocean (NI), the Somalian low-level coastal jet and the Indian monsoon have a clear impact on the swell probability pattern. The NI, with the exception of the summer monsoon period (JJA), is the most swell-dominated area of the World Ocean. When the three main oceans are compared, the PO has the highest swell probability (91.7%), followed by the IO (91.2%) and the AO (87.0%).

4. Interannual variability of the wave heights

a. Basinwide EOFs

To obtain the main patterns of the interannual variability of the wave fields, we performed an empirical orthogonal function (EOF) analysis (e.g., von Storch

TABLE 1. Seasonal variations of the swell probability.

Hemisphere	Basin	Swell probability – P_s (%)				
		DJF	MAM	JJA	SON	Total
North	NA	84.3	87.0	88.8	87.2	86.9
	NP	88.2	91.7	94.1	90.8	91.3
	NI	94.5	97.7	89.8	97.2	94.8
	Total	86.3	89.7	91.2	89.1	89.2
South	South Atlantic	89.2	87.9	84.6	84.3	87.4
	South Pacific	93.1	92.0	90.2	91.3	91.7
	South Indian	92.2	90.9	89.1	89.4	90.7
	Total	91.9	90.7	88.6	89.2	90.4
Global		89.7	90.2	89.5	89.0	89.8

and Zwiers 1999) to the H_s , H_s^s , and H_s^w detrended seasonal mean fields. The time series of the empirical orthogonal functions, the principal components (PCs), are normalized to have unit variance, so that the corresponding EOFs represent the typical variability of the data in their original units. To avoid the masking of *interocean* variability, but still retaining the north–south swell propagation pattern from opposite hemispheres, we analyze the three major ocean basins, including their SO sectors, separately. The first two EOF spatial patterns (EOF1 and EOF2) were computed for DJF and JJA. Only the EOF1s are shown here. The percentages of the explained variances are shown in Table 2, together with those from an analysis of the NP, NA, and SO alone, used later in this study.

Figures 7 and 8 show the DJF and JJA H_s , H_s^s , and H_s^w EOF1 spatial patterns. In the PO and AO, the spatial patterns of the leading modes are qualitatively comparable with each other in both seasons. In DJF the PO and AO EOF1 patterns of H_s are formed by dominating anomalies of one sign and lower magnitude anomalies of the opposite sign in the western PO and in the Bering Sea and in the western NA, respectively. The maxima of the explained variances are located in the northern subpolar latitudes, in the central and eastern NP and NA. The EOF1 spatial patterns of H_s^s in the PO and AO are also formed by dominating anomalies of the same sign. These patterns clearly represent the eastward- and southward-propagating swell, away from the generation areas in DJF. The southward extension of the leading swell patterns reaches about 60°S in DJF, propagating as far as the west coast of Chile in the PO and the coasts of Namibia and South Africa in the AO. Not surprisingly, the southward propagation of swell is more prominent in the PO. Although the geography of the AO limits southward swell propagation, swell waves generated in the NA clearly reach the southern AO, in line with Alves (2006). In the same season, the patterns of the EOF1s of H_s^w are characterized by a well-defined meridional tripole in the NP and NA. The maxima of explained variances are located

TABLE 2. Explained variance of EOF1 and EOF2 (%).

Ocean/basin	EOF1						EOF2					
	DJF			JJA			DJF			JJA		
	H_s	H_s^s	H_s^w									
PO	25.7	37.8	12.7	31.6	38.6	18.6	—	—	—	—	—	—
AO	25.3	32.4	19.7	30.1	43.0	14.5	—	—	—	—	—	—
IO	28.5	40.7	27.2	34.7	50.0	24.1	—	—	—	—	—	—
NP	36.7	47.6	23.1	28.2	41.3	17.7	15.0	13.5	13.2	20.3	19.3	8.5
NA	32.9	40.8	26.7	31.6	44.4	17.3	30.5	29.7	16.0	14.4	13.3	11.3
SO	39.0	47.0	29.2	33.0	37.0	23.5	11.1	13.5	8.2	17.5	19.7	12.6

between 30° and 35°N, with anomalies of the opposite sign north and south of these areas.

The main patterns of variability of H_s , H_s^s , and H_s^w in the IO are different from those in the PO and AO. In DJF the EOF1 spatial pattern of H_s in the IO exhibits a tripole structure centered around 40°S and is qualitatively more in line with the structure of the DJF H_s^w variability pattern than in the remaining oceans. In the IO the DJF EOF1 H_s^s pattern is formed by low-magnitude anomalies of the same sign throughout the whole basin, reflecting the northward swell propagating away from the generation area located around 45°S.

The EOF1 patterns of H_s , H_s^s , and H_s^w in the PO and AO in JJA are more or less symmetric to DJF. One noticeable difference is that anomalies of the opposite sign in the summer (northern) hemisphere are now more dominant. As in DJF, the JJA H_s^s EOF1 patterns in the PO and AO clearly show swell propagating away from the wave-generation area in the SO. The northward-bound swell penetration in the AO is now more confined to the South Atlantic. As in DJF, but now in the SH, the JJA EOF1s of H_s^w are characterized by a meridional tripole. The maxima of explained variance are located between 30° and 35°S in both oceans. In the IO the main patterns of variability of H_s , H_s^s , and H_s^w exhibit larger anomalies in JJA than in DJF because of the SH winter season. The pattern of the leading mode of H_s^s is formed by anomalies of the same sign throughout the whole basin. Its center of action is shifted eastward with respect to the H_s EOF1 pattern and extends from the Kerguelen Islands to the Australian Bight.

b. Connection between the wave field variability and large-scale atmospheric circulation

To analyze the association between the wave height variability and the atmospheric circulation patterns, an additional EOF analysis was carried out for the NA and NP and for the SO. The spatial patterns of these regional EOFs (not shown) are similar to the full-basin EOFs, but their explained variances are slightly different. The atmospheric circulation patterns are represented by the

following atmospheric indices (the atmospheric drivers): the NA Oscillation (NAO; Hurrell 1995), the NP index (NPI; Trenberth and Hurrell 1994), the Southern Oscillation index (SOI; Ropelewski and Jones 1987), and the southern annular mode index (SAM; Marshall 2003). The strength of the NA and northeastern Pacific westerlies can be deduced from the NAO index and from the NPI, respectively. The intensity of the extratropical circulation in the PO is related to the Southern Oscillation, represented by the SOI, through the mechanism of the “atmospheric bridge” (Alexander et al. 2002). The SAM represents the principal mode of variability in the atmospheric circulation of the SO extratropics and high latitudes and is related to the SO belt wind regime (Hurrell and van Loon 1994).

Figure 9 displays the H_s , H_s^s , and H_s^w normalized PCs from the NA wave EOF1s and the NAO index. The December 1991–May 1993 period was deleted from the analysis (see section 2). Table 3 displays the correlation coefficients between pairs of the wave height PCs with each other and with the detrended NAO index. Generally, the correlations between the PCs of H_s and H_s^s are very high, those between the H_s^s and H_s^w are low, and those between the H_s and H_s^w are in between the other two. The same applies to the NP and the SO (see Tables 4 and 5). Wind-sea and swell waves are physically independent, and their maxima occur in different regions (see Figs. 2 and 3); therefore, their low correlations are not surprising. Conversely, H_s^w and H_s^s add to the total H_s , so they must be correlated to the latter to some extent. Since the wave field is dominated by swell (see above), the correlation between H_s and H_s^s is highest. The correlations between H_s and H_s^w are higher in the respective winter hemisphere, reflecting the lower swell dominance in the winter.

In the NA the H_s^w PC1 is highly correlated with the NAO index in DJF ($r = 0.84$) but not in JJA ($r = 0.07$). This is not surprising, as the NAO is predominantly a winter phenomenon. The agreement between the H_s and H_s^s PC1s and the NAO index in DJF is low ($r = 0.30$ and $r = 0.26$, respectively). The DJF H_s^w EOF1 spatial pattern in the NA region exhibits a NAO-like structure (Fig. 7).

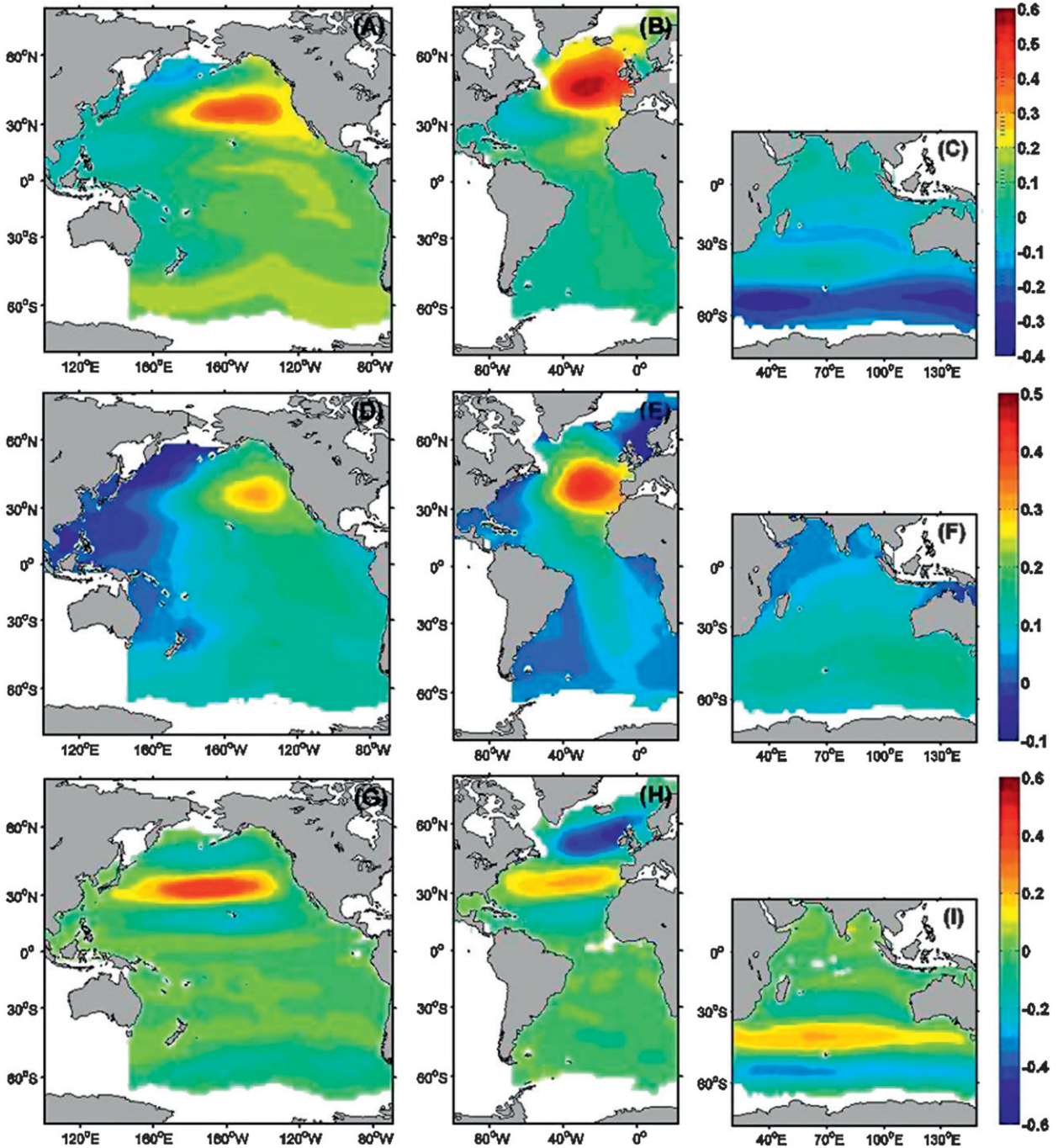


FIG. 7. First EOFs of DJF detrended (a)–(c) H_s , (d)–(f) H_s^S , and (g)–(i) H_s^W for the PO, AO, and IO. The color scales vary between the panels.

The H_s^S EOF1 spatial pattern in the same season clearly represents swell propagating away from the storm-track region and does not resemble the NAO structure. Since H_s is dominated by swell, its PC1 is also not related to the NAO. The DJF H_s and H_s^S PC2s have a correlation of 0.85 and 0.87, respectively, with the NAO index. These results are in line with Sterl and Caires (2005) and Bauer (2001)

but not with GG06. The leading variability modes of the wind-sea and swell heights from VOS are more correlated with each other and therefore swell “follows” the wind-sea pattern and its NAO-like structure. A possible explanation for this is that the subjective judgment of the observer is intuitively driven to correlate wind sea and swell in his visual estimates of the wave heights.

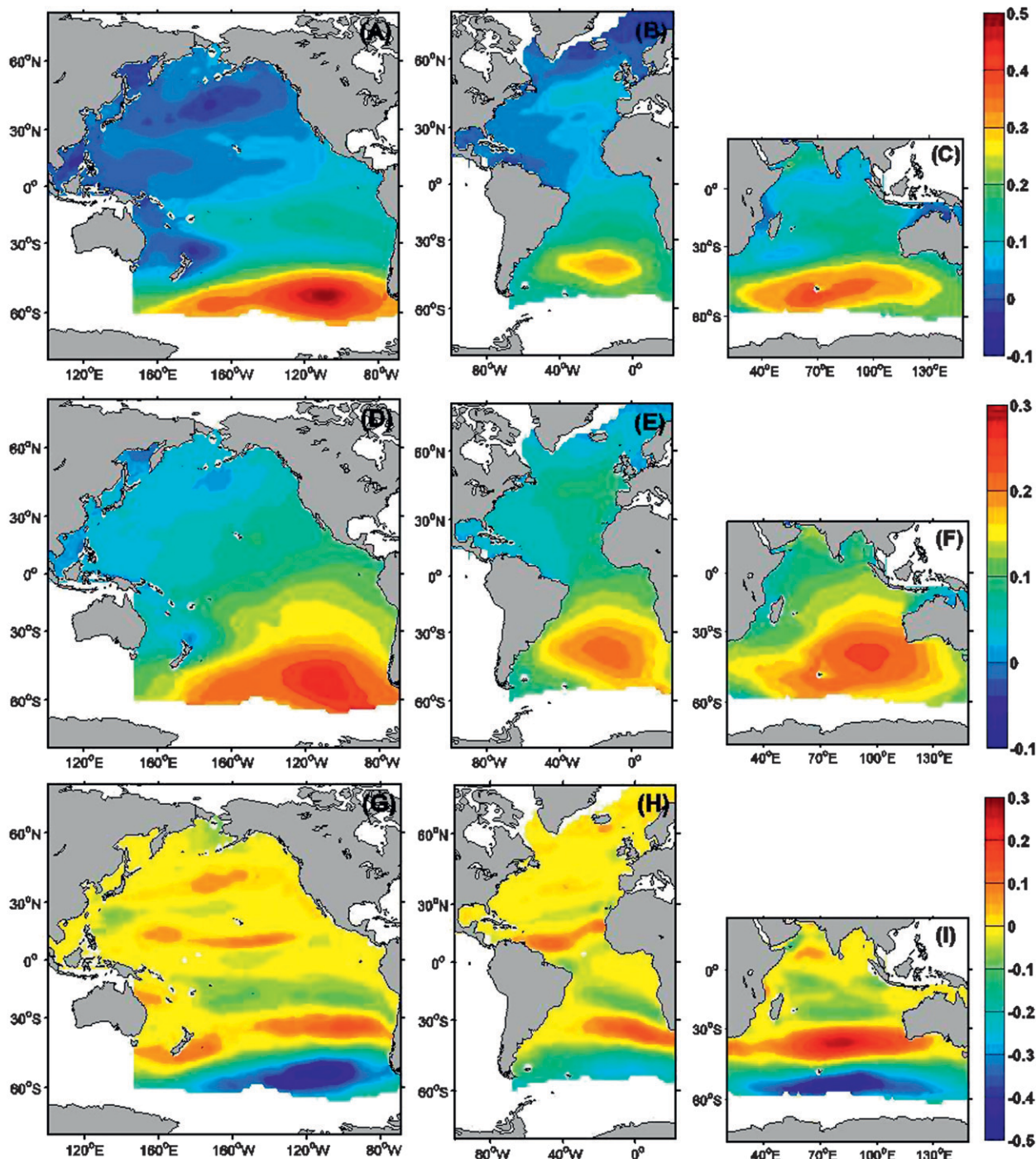


FIG. 8. As in Fig. 7, but for JJA.

The PC1s of the normalized DJF and JJA H_s , H_s^s , and H_s^w first leading modes in the NP are shown in Fig. 10, along with the NPI and SOI. The correlation coefficients between the different time series are shown in Table 4. The correlation between H_s , H_s^s , and H_s^w PC1s and the detrended NPI is high in DJF ($r = 0.83$, $r = 0.79$, and

$r = 0.78$, respectively) but low in JJA ($r < 0.3$). The correlations between the H_s and H_s^s PC2s and the NPI are low in both seasons and between the H_s^w PC2s and the NPI is high ($r > 0.5$), also in both seasons. The DJF results are in line with GG06, although our results show a slightly higher correlation between the leading wave

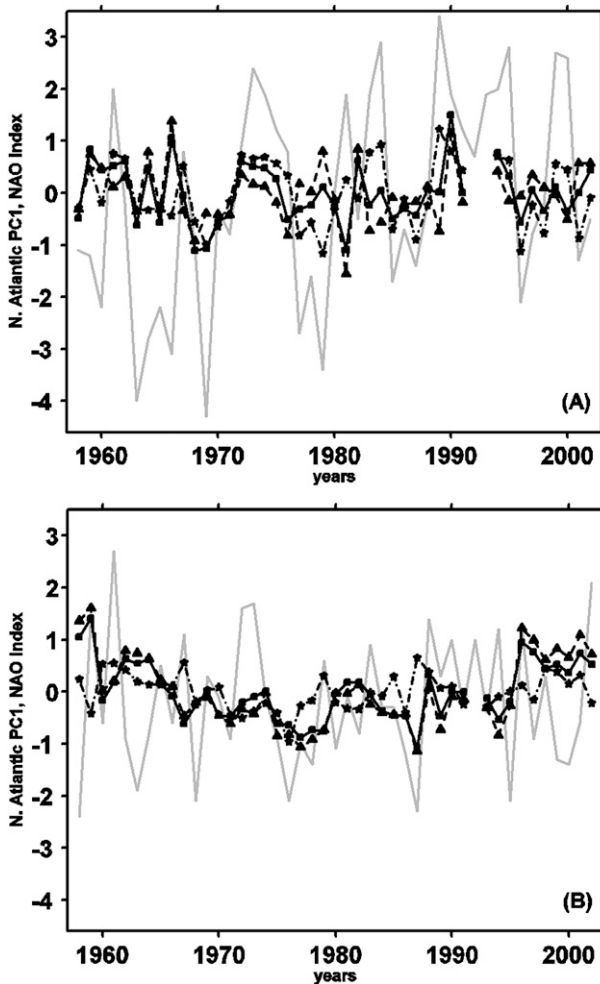


FIG. 9. First normalized PCs of (a) DJF and (b) JJA detrended H_s (full line with squares), H_s^s (dashed line with triangles), and H_s^w (dotted-dashed line with stars), in the NA, along with the NAO index (gray line).

heights PCs and the NPI. The correlation between the detrended SOI and the wave heights PCs is relatively low. The exceptions are H_s and H_s^s in DJF ($r = 0.57$ in both cases) and the H_s^w PC2 ($r = 0.57$). The Southern Oscillation does have some impact on the NP wave height variability modes (stronger in DJF), most likely because of swell waves generated along the trade winds.

Figure 11 and Table 5 show the same information for the SO, with the detrended SAMI replacing the NPI and the SOI. The correlations between the H_s^w PC1s and the SAMI are higher in DJF ($r = 0.73$) than in JJA ($r = 0.49$). The correlation between the H_s^s PC1s and the SAMI is relatively high in DJF ($r = 0.60$) but lower in JJA ($r = 0.28$), and the agreement between the H_s PC1s and the SAMI, in both seasons, has a similar behavior ($r = 0.57$ in DJF and $r = 0.37$ in JJA). The correlations between the wave heights PCs and the SAMI in the SO sectors (not

TABLE 3. Correlation coefficients for PC1 and PC2 of H_s , H_s^s , and H_s^w in the NA, with each other and with the detrended NAO index for DJF and JJA.

Pairs of parameters	EOF1		EOF2	
	DJF	JJA	DJF	JJA
$H_s^w - H_s^s$	0.13	0.24	0.26	0.63 ^a
$H_s^w - H_s$	0.48 ^b	0.14	0.56 ^a	0.68 ^a
$H_s^s - H_s$	0.81 ^a	0.98 ^a	0.88 ^a	0.98 ^a
$H_s^w - \text{NAO}$	0.84 ^a	0.07	0.26	0.51 ^a
$H_s^s - \text{NAO}$	0.30 ^c	0.08	0.87*	0.59 ^a
$H_s - \text{NAO}$	0.26	0.15	0.85*	0.56 ^a

^a Significant at the 99% level.

^b Significant at the 95% level.

^c Significant at the 90% level.

shown) are similar. Our correlations between the H_s PCs and the SAMI are generally in qualitative agreement with Hemer et al. (2010). An exception is the high correlation between the H_s PC1 and the SAMI that we find in DJF (actually higher than in JJA).

5. Long-term variability analysis

Observations from different sources, including modeling reanalyses (WASA Group 1998; Gulev and Hasse 1999; Wang and Swail 2001; GG06; Bromirski et al. 2005), suggest that wave heights in the NP and NA increased during the last quarter-century. This feature is not exclusive to the NH, since in the SH wave heights have also been increasing since 1975 (Hemer et al. 2010). By averaging the global ERA-40 U_{10} and H_s , Sterl and Caires (2005) showed that wave heights have actually increased globally, almost steadily, since 1975, and that these changes are linked to an increase in the global U_{10} . But, as previously mentioned, the global wave field is complex and owing to swell propagation, this increase is not uniform and is not necessarily directly linked to the local U_{10} variability.

Because of the caveats mentioned in section 2, the uncorrected ERA-40 wave height data for climate variability studies should be used with caution. However, ERA-40 is the best long-term wave reanalysis available, and it compares better with observations in terms of rmse index than any other reanalysis (Caires et al. 2004). Furthermore, it is the only global dataset, besides the visual wave height estimates from VOS, with separated wind-sea and swell parameters. The ERA-40 problems are due to inhomogeneities and undersampling of assimilated data and are the largest in the SH; therefore, here we focus on the DJF H_s^s and H_s^w long-term variability in the NP and NA only and on how these changes combine and link to the overall H_s long-term variability.

TABLE 4. As in Table 3, but in the NP and with the detrended NPI and SOI.

Pairs of parameters	EOF1		EOF2	
	DJF	JJA	DJF	JJA
$H_s^w - H_s^s$	0.54 ^a	-0.05	0.35 ^b	0.39 ^b
$H_s^w - H_s$	0.64 ^a	0.03	0.35 ^b	0.52 ^a
$H_s^s - H_s$	0.99 ^a	0.99 ^a	0.47 ^c	0.94 ^a
$H_s^w - \text{NPI}$	0.78 ^a	0.06	0.61 ^a	0.51 ^a
$H_s^s - \text{NPI}$	0.79 ^a	0.23	0.02	0.10
$H_s - \text{NPI}$	0.83 ^a	0.29	0.37 ^b	0.15
$H_s^w - \text{SOI}$	0.28	0.18	0.57 ^a	0.37 ^b
$H_s^s - \text{SOI}$	0.57 ^a	0.38 ^b	0.37 ^b	0.19
$H_s - \text{SOI}$	0.57 ^a	0.41 ^c	0.05	0.21

^a Significant at the 99% level.

^b Significant at the 90% level.

^c Significant at the 95% level.

The DJF patterns of the H_s , H_s^s , and H_s^w linear trends in the NP and NA, together with their statistical significance, are shown in Fig. 12. The statistical significance was computed using a Student's t test, and additionally analyzed using the Hayashi (1982) criterion, which considers the confidence intervals of the statistical significance. If $|R| \gg 1$, then the true value is close to its estimate; if $|R| \leq 1$, then the confidence interval can be very wide, even if the Student's t test is satisfied (R is the Hayashi "reliability ratio"). The linear trends of H_s^s show that the largest upward changes in the NP coincide with the extratropical storm-track area, with a maximum increase of the order of 12–14 cm decade⁻¹. Along the West Coast of the United States, a lower increase in H_s^s of 7–10 cm decade⁻¹ is found. The pattern of the H_s^w linear trends is similar, although with a smaller increase (8–10 cm decade⁻¹). Small but statistically significant increases of H_s^s and H_s^w can be seen in the tropics and in the low latitudes. A small decrease is noticeable along the west coasts of Mexico and Central America. Since in the NP the long-term trends of H_s^s and H_s^w are more or less collocated, their positive changes add up and the resulting variation of H_s has a maxima located along the extratropical storm path as well (16–20 cm decade⁻¹).

GG06 have also studied the long-term variability of swell and wind-sea heights in the NP and NA from VOS estimates. Their NH winter is JFM, and their data period is 1958–2002. We have computed linear wave height trends for the same period (not shown). Our results are qualitatively in line with GG06. Our patterns of the secular changes are similar to theirs but with systematically lower tendencies. Our results are more in line with the H_s long-term tendencies computed by Caires and Swail (2004), from the corrected ERA-40 data. They reported the highest increase in the NP of 24 cm decade⁻¹, about 3 cm decade⁻¹ larger than our results. The cause for this

TABLE 5. Correlation coefficients of the first and second PCs of H_s , H_s^s , and H_s^w , in the Southern Ocean belt with each other and with the detrended SAMI, for DJF and JJA.

Pairs of parameters	EOF1		EOF2	
	DJF	JJA	DJF	JJA
$H_s^w - H_s^s$	0.49 ^a	0.58 ^b	0.04	0.39 ^c
$H_s^w - H_s$	0.78 ^b	0.75 ^b	0.22	0.21
$H_s^s - H_s$	0.92 ^b	0.97 ^b	0.87 ^b	0.94 ^b
$H_s^w - \text{SAMI}$	0.73 ^b	0.49 ^a	0.04	0.14
$H_s^s - \text{SAMI}$	0.60 ^b	0.28	0.11	0.27
$H_s - \text{SAMI}$	0.57 ^b	0.37 ^c	0.03	0.11

^a Significant at 95% level.

^b Significant at 99% level.

^c Significant at 90% level.

difference is rooted in the underestimation of high wave heights in the uncorrected ERA-40 used in the present study. Since H_s is dominated by swell, one would expect H_s^s to have a slightly higher long-term tendency.

The largest upward changes in the NA H_s^s field are found in the northeastern part of the subbasin, particularly between Iceland and the British Isles (14–18 cm decade⁻¹), but also in the central midlatitudes (8–12 cm decade⁻¹) and in the Norwegian Sea (16–20 cm decade⁻¹). Small but statistically significant increases of H_s^s are also present in the tropics and in the low latitudes. The upward changes in the H_s^w are largest in the central midlatitudes (about 10–12 cm decade⁻¹) and coincide with the DJF mean climatological maxima of U_{10} and H_s^w (see above). Small increases are also present in the North Sea and in the southwest tropics. Very small increases, or even some light minor decreases, of H_s^w can be seen in the Norwegian Sea and close to the equator. The combined effect of the NA H_s^s and H_s^w linear trends on the long-term changes of H_s result in the largest upward changes occurring throughout the central midlatitudinal NA, toward the west coast of the British Isles (in excess of 18 cm decade⁻¹) and in the Norwegian Sea (12–14 cm decade⁻¹). As for the NP, our spatial patterns of the linear trends for JFM are qualitatively in line with GG06; however, our positive trends in the NA are systematically lower than those computed by GG06 and are also more in line with the tendencies from Caires and Swail (2004), who obtain 25 cm decade⁻¹, which is about 5 cm higher than our results.

The spatial patterns of the H_s^s and H_s^w linear trends are less consistent with each other in the NA than in the NP. A possible explanation for this difference, as pointed out by GG06, is that swell propagates away northeastward, from the areas of highest wind-sea changes, resulting in a pattern of shifted swell variability into the Norwegian Sea. The northeastward swell propagation pattern away from the extratropical storm track is less predominant in the NP than in the NA.

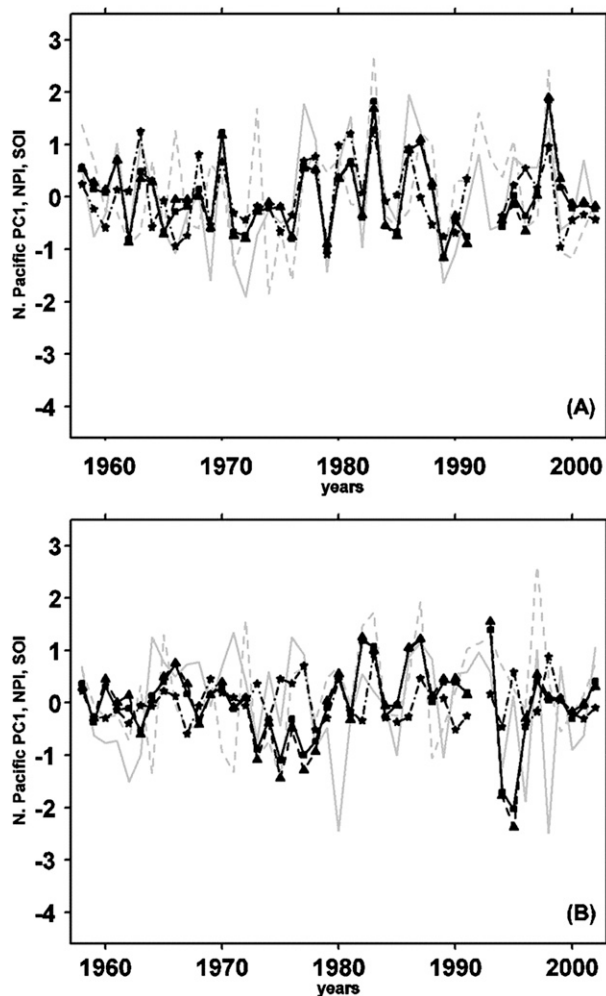


FIG. 10. As in Fig. 9, but for the NP, along with the NPI (gray line) and SOI (dashed gray line).

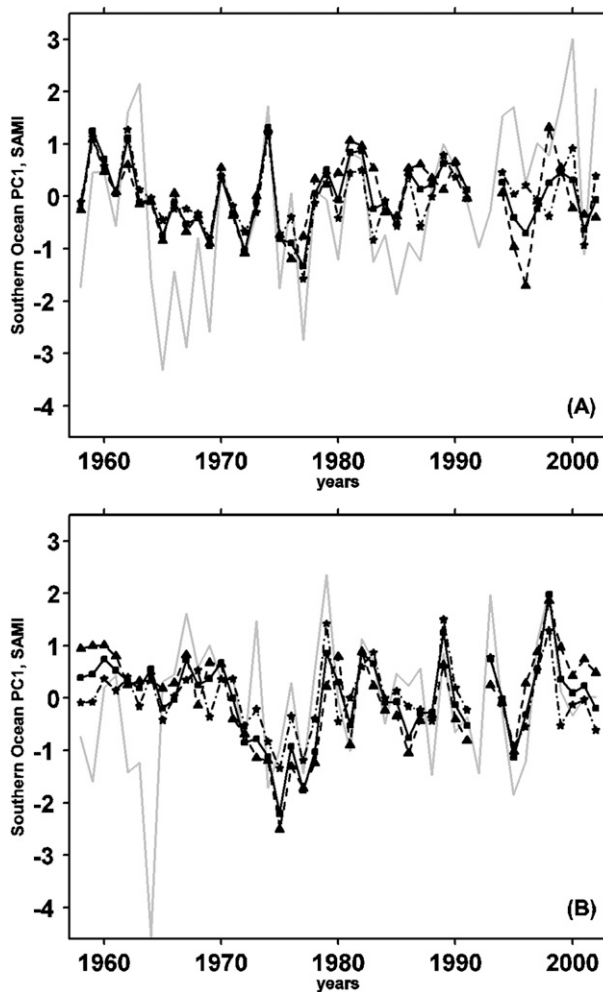


FIG. 11. As in Fig. 10, but in the Southern Ocean belt, along with the SAMI (gray line).

Figure 13 displays time series of H_s , H_s^s , and H_s^w averaged over the areas $30^\circ\text{--}54^\circ\text{N}$, $140^\circ\text{--}165^\circ\text{W}$ in the NP and $40^\circ\text{--}64^\circ\text{N}$, $10^\circ\text{--}30^\circ\text{W}$ in the NA. In the northeast Pacific, the wave heights have a consistent positive trend: $1.0\% \text{ yr}^{-1}$ for H_s^s and $0.43\% \text{ yr}^{-1}$ for H_s^w . The H_s upward trend ($1.18\% \text{ yr}^{-1}$) is more in line with the H_s^s trend. These tendencies are qualitatively in line with buoy measurements from Bromirski et al. (2005).

The H_s^s trend in the northwest Atlantic is $0.97\% \text{ yr}^{-1}$ and is also higher than the H_s^w trend, which is $0.49\% \text{ yr}^{-1}$. The resulting H_s upward trend for the same area is $1.15\% \text{ yr}^{-1}$ and, like in the NP, is more in line with the H_s^s trend. Buoy records from Bacon and Carter (1993) show similar upward tendencies (about $1\% \text{ yr}^{-1}$). GG06 used a similar approach, although in slightly different areas. We have computed the linear wave height trends using their areas and the JFM period (not shown). In the NP our trends are qualitatively similar, showing well

defined but slightly smaller upward trends. In the NA our trends for H_s and H_s^s are also qualitatively very similar, while those for H_s^w differ. While we find a consistent increase of $0.63\% \text{ yr}^{-1}$, GG06 obtained a well-defined decreasing linear trend in this parameter, in particular after 1970. Our H_s^w linear trend is in line with the U_{10} upward changes ($1.1\% \text{ yr}^{-1}$) in the same region and for the same period.

6. Summary and conclusions

A detailed climatology of the DJF and JJA wave heights and directions is presented. The analysis is done for wind sea and swell separately. Additionally, we show the seasonal spatial distribution of the wind-sea and swell wave energy fluxes (power) fields. The global wave field is found to be dominated by swell, even along the extratropical storm areas, where the relative weight of

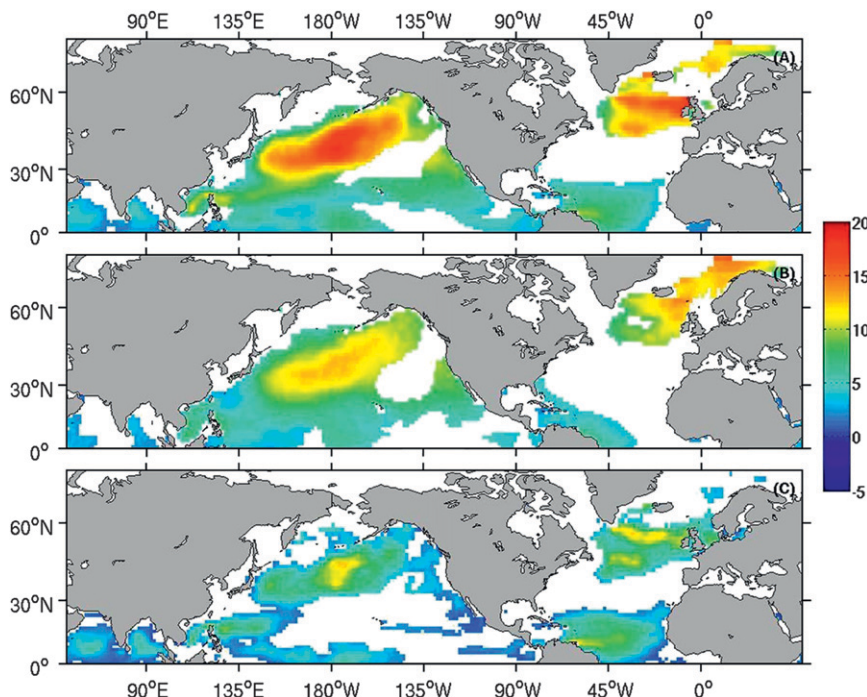


FIG. 12. Linear trends (cm decade^{-1}) in DJF of (a) H_s , (b) H_s^s , and (c) H_s^w for the NP and NA. Only linear trends significant at the 95% level and that fulfill the Hayashi criterion are shown.

the wind-sea part of the wave spectra is highest. In the low latitudes, the swell dominance is almost permanently close to 100%. The swell energy dominates the overall wave energy field. The DJF and JJA H_s^s and H_s^w fields (Figs. 2 and 3) are influenced by the choice of the spectral partitioning scheme used in ERA-40 (see section 2), and the use of alternative partitioning schemes (Loffredo et al. 2009) may change details of the results. However, the swell dominance of the wave field is so strong that it is hard to believe that a different partitioning scheme would yield completely different results. The study of the role of different spectral partitioning schemes on wind-sea and swell climates is left for future research. Although the global ocean is clearly dominated by swell, it should also be pointed out that swell waves have different natures and have different impacts on the MABL and ocean mixing layer, depending on their age and distance to the generating storm.

We compare our results with previous studies of wind-sea and swell climate and variability. Despite the use of different wave datasets, such as visual VOS estimates (GGSW03) or remote sensing (CCEV02) and different wind sea–swell separation criteria, the agreement is generally good. The previously identified caveats of the VOS estimates in the SO, which result from under-sampling, and the general underestimation of the uncorrected ERA-40 wave heights are confirmed.

The interannual variability of the wind-sea and swell significant wave heights is investigated by means of an EOF analysis. It is shown that because of the swell dominance of the wave field, the SWH variability is mostly controlled by the variability of swell.

To analyze the potential mechanisms behind the interannual variability of wind sea and swell, their relation with the atmospheric forcing is studied. In the NH the influence of the large-scale atmospheric forcing is found to be more important during DJF than during JJA. In the SH, the strength of the SO wind speed as represented by the SAMI is shown to be an important driving force behind the wave climate variability independent of the season.

In both the NA and NP, a positive long-term trend in the H_s^s and H_s^w fields is found. The resulting variation patterns of H_s are also positive, and these changes are mainly related to the increase of H_s^s . The patterns of the linear trends of H_s^s and H_s^w are similar in the NP, while they differ in the NA. The similarity of the changes in H_s and H_s^s suggests that the recent increase in the storm frequency (Gulev et al. 2001; GG06) in the NA plays an important role in the increase of H_s . The same conclusion can be drawn for the NP in view of the GG06 findings. Although the long-term variability analysis may suffer from the wave height underestimation in ERA-40, our results are qualitatively in line with the tendencies computed from the corrected H_s by Caires and Swail (2004).

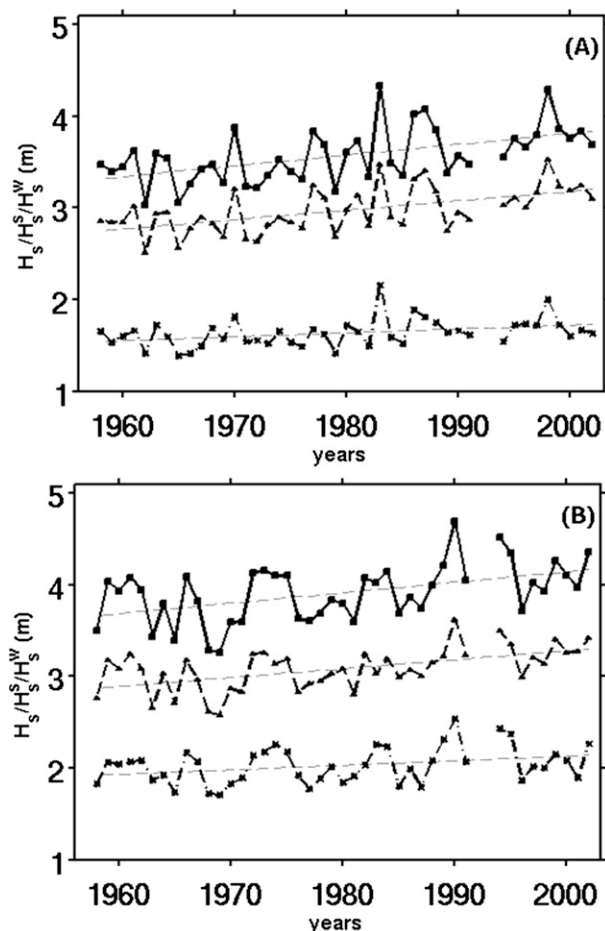


FIG. 13. Time series of DJF H_s^w (full line with squares), H_s^s (dashed line with triangles), and H_s^w/H_s^s (dotted-dashed line with stars) linear trends in the area bounded by (a) 30°–54°N, 140°–165°W in the NP and (b) 40°–64°N, 10°–30°W in the NA.

The recent increase in the wave heights is more intense in the respective winter hemisphere. Because of swell propagation, this increase has an impact not only on the H_s^s field in the opposite hemisphere but also in the T_m^s field. Future analysis of the variability of wind sea and swell should address the tendencies of T_m^s and wave power (or wave energy flux), since changes in the energy potential of very long swells generated in the winter hemisphere can pose a considerable danger to coastal and offshore structures.

Future changes in surface ocean wave conditions received little attention in the Intergovernmental Panel on Climate Change (PCC) Fourth Assessment Report (AR4), and studies of the impact of future climate changes due to global warming on the wave field are presently a concern in the wave climate community (Hemer et al. 2010). Global wave climate projections using wave models forced by GCMs (global climate models) wind projections should therefore be pursued to assess the impact of changes

in extratropical storms' strength and track (Bengtsson et al. 2009) on the global wave field conditions.

The WAM has undergone substantial improvements since ERA-40, resulting in a more realistic interaction between wind sea and swell and better forecasting scores (Bidlot et al. 2007). The improved WAM is used in the ERA-Interim, the new ECMWF reanalysis (Simmons et al. 2006). The ERA-Interim covers a period from 1989 onward and is continued in near-real time. Future and complementary analysis on the validation of the ERA-Interim wave parameters, including the wind-sea and swell balance, and on the wave climate changes since 2002 should be addressed. A recent analysis of the trends in some atmospheric parameters (Simmons et al. 2010) indicates a leveling after about 1998. Whether this is also the case for the wave field parameters should also be addressed in future research.

Acknowledgments. Alvaro Semedo and Kay Sušelj were funded by the European Commission's ModObs project under Contract MRTN-CT-2005-019369. We greatly appreciated the help of Jean Bidlot from ECMWF (Reading, United Kingdom) with the many details of the ERA-40 wave data.

REFERENCES

- Alexander, M. A., I. Blade, M. Newman, J. Lanzante, N.-C. Lau, and J. D. Scott, 2002: The atmospheric bridge: The influence of the ENSO teleconnections on air-sea interaction over the global oceans. *J. Climate*, **15**, 2205–2231.
- Alves, J. H. G. M., 2006: Numerical modeling of ocean swell contributions to the global wind-wave climate. *Ocean Modell.*, **11**, 98–122.
- Arduin, F., B. Chapron, and F. Collard, 2009: Observation of swell dissipation across oceans. *Geophys. Res. Lett.*, **36**, L06607, doi:10.1029/2008GL037030.
- Bacon, S., and D. J. T. Carter, 1993: A connection between mean wave height and atmospheric pressure gradient in the North Atlantic. *Int. J. Climatol.*, **13**, 423–436.
- Barber, N. F., and F. Ursell, 1948: The generation and propagation of ocean waves and swell. I. Wave periods and velocities. *Philos. Trans. Roy. Soc. London*, **A240**, 527–560.
- Barstow, S. F., 1996: World wave atlas. *AVISO Newsletter*, No. 4, AVISO, Ramonville St-Agne, France, 24–35.
- Bauer, E., 2001: Interannual changes of the ocean wave variability in the North Atlantic and in the North Sea. *Climate Res.*, **18**, 63–69.
- , M. Stolley, and H. von Storch, 1997: On the response of surface waves to accelerating the wind forcing. GKSS Manuscript 96/E/89, 24 pp.
- Bengtsson, L., K. I. Hodges, and N. Keenlyside, 2009: Will extratropical storms intensify in a warmer climate? *J. Climate*, **22**, 2276–2301.
- Bidlot, J.-R., 2001: ECMWF wave model products. *ECMWF Newsletter*, No. 91, ECMWF, Reading, United Kingdom, 9–15.
- , P. Janssen, and S. Abdalla, 2007: A revised formulation of ocean wave dissipation and its model impact. ECMWF Tech. Memo. 509, 29 pp. [Available online at <http://www.ecmwf.int/publications/>.]

- Bromirski, P. D., D. R. Cayan, and R. E. Flick, 2005: Wave spectral energy variability in the northeast Pacific. *J. Geophys. Res.*, **110**, C03005, doi:10.1029/2004JC002398.
- Caires, S., and A. Sterl, 2003: Validation of ocean wind and wave data using triple collocation. *J. Geophys. Res.*, **108**, 3098, doi:10.1029/2002JC001491.
- , and V. Swail, 2004: Global wave climate trend and variability analysis. *Proc. Eighth Int. Workshop on Wave Hindcasting and Forecasting*, Oahu, HI, U.S. Army Engineer Research and Development Center's Coastal and Hydraulics Laboratory and Cosponsors, AI. [Available online at <http://www.waveworkshop.org/8thWaves/Papers/A1.pdf>.]
- , and A. Sterl, 2005: 100-year return value estimates for ocean wind speed and significant wave height from the ERA-40 data. *J. Climate*, **18**, 1032–1048.
- , —, J.-R. Bidlot, N. Graham, and V. Swail, 2004: Intercomparison of different wind wave reanalyses. *J. Climate*, **17**, 1893–1913.
- , —, and C. P. Gommenginger, 2005: Global ocean mean wave period data: Validation and description. *J. Geophys. Res.*, **110**, C02003, doi:10.1029/2004JC002631.
- Cavaleri, L., 2009: Wave modeling—Missing the peaks. *J. Phys. Oceanogr.*, **39**, 2757–2778.
- Chen, G., B. Chapron, R. Ezraty, and D. Vandemark, 2002: A global view of swell and wind sea climate in the ocean by satellite altimeter and scatterometer. *J. Atmos. Oceanic Technol.*, **19**, 1849–1859.
- Donelan, M. A., W. M. Drennan, and K. B. Katsaros, 1997: The air–sea momentum flux in conditions of wind sea and swell. *J. Phys. Oceanogr.*, **27**, 2087–2099.
- Gerling, T. W., 1992: Partitioning sequences and arrays of directional wave spectra into component wave systems. *J. Atmos. Oceanic Technol.*, **9**, 444–458.
- Grachev, A. A., and C. W. Fairall, 2001: Upward momentum transfer in the marine boundary layer. *J. Phys. Oceanogr.*, **31**, 1698–1711.
- Gulev, S. K., and L. Hasse, 1998: North Atlantic wind waves and wind stress fields from voluntary observing data. *J. Phys. Oceanogr.*, **28**, 1107–1130.
- , and —, 1999: Changes of wind waves in the North Atlantic over the last 30 years. *Int. J. Climatol.*, **19**, 1091–1117.
- , and V. Grigorieva, 2004: Last century changes in ocean wind wave height from global visual wave data. *Geophys. Res. Lett.*, **31**, L24302, doi:10.1029/2004GL021040.
- , and —, 2006: Variability of the winter wind waves and swell in the North Atlantic and North Pacific as revealed by the voluntary observing ship data. *J. Climate*, **19**, 5667–5685.
- , O. Zolina, and S. Grigoriev, 2001: Extratropical cyclone variability in the NH winter from the NCEP/NCAR reanalysis data. *Climate Dyn.*, **17**, 795–809.
- , V. Grigorieva, A. Sterl, and D. Woolf, 2003: Assessment of the reliability of wave observations from voluntary observing ships: Insights from the validation of a global wind wave climatology based on voluntary observing ship data. *J. Geophys. Res.*, **108**, 3236, doi:10.1029/2002JC001437.
- Hanson, J. L., and O. M. Phillips, 2001: Automated analysis of ocean surface directional wave spectra. *J. Atmos. Oceanic Technol.*, **18**, 277–293.
- Hayashi, Y., 1982: Confidence intervals of a climatic signal. *J. Atmos. Sci.*, **39**, 1895–1905.
- Hemer, M. A., J. A. Church, and J. R. Hunter, 2010: Variability and trends in the directional wave climate of the Southern Hemisphere. *Int. J. Climatol.*, **30**, 475–491.
- Hogben, N., 1995: Increases in wave heights over the North Atlantic: A review of the evidence and some implications for the naval architect. *Trans. Roy. Inst. Nav. Archit.*, **137A**, 93–115.
- , N. M. C. Dacunka, and G. F. Oliver, 1986: *Global Wave Statistics*. Unwin Brothers, 661 pp.
- Högström, U., A. Smedman, E. Sahlée, W. M. Drennan, K. K. Kahma, H. Pettersson, and F. Zhang, 2009: The atmospheric boundary layer during swell: A field study and interpretation of the turbulent kinetic energy budget for high wave ages. *J. Atmos. Sci.*, **66**, 2764–2779.
- Holthuijsen, L. H., 2007: *Waves in Oceanic and Coastal Waters*. Cambridge University Press, 387 pp.
- Hurrell, J. W., 1995: Decadal trends in the North Atlantic Oscillation: Regional temperatures and precipitation. *Science*, **269**, 676–679.
- , and H. van Loon, 1994: A modulation of the atmospheric cycle in the Southern Hemisphere. *Tellus*, **46A**, 325–338.
- Komen, G. J., L. Cavaleri, M. Doneland, K. Hasselmann, S. Hasselmann, and P. A. E. M. Janssen, Eds., 1994: *Dynamics and Modelling of Ocean Waves*. Cambridge University Press, 532 pp.
- Korevaar, C. G., 1990: *North Sea Climate: Based on Observations from Ships and Light Vessels*. Kluwer Academic, 137 pp.
- Loffredo, L., J. Monbaliu, E. Bitner-Gregersen, and A. Toffoli, 2009: The role of spectral multimodality in wave climate design. *Proc. 11th Int. Workshop on Wave Hindcasting and Forecasting and Coastal Hazard Symp.*, Halifax, NS, Canada, 10 pp. [Available online at http://www.waveworkshop.org/11thWaves/Papers/Loffredo_etal_2009.pdf.]
- Marshall, G. J., 2003: Trends in the southern annular mode from observations and reanalyses. *J. Climate*, **16**, 4134–4143.
- Munk, W. H., 1944: Proposed uniform procedure for observing waves and interpreting instrument records. Scripps Institution of Oceanography, Wave Project Rep. 26, 22 pp.
- , G. R. Miller, F. E. Snodgrass, and N. F. Barber, 1963: Directional recording of swell from distant storms. *Philos. Trans. Roy. Soc. London*, **A255**, 505–584.
- Pierson, W. J., and L. Moskowitz, 1964: A proposed spectral form for fully developed wind seas based on the similarity theory of S. A. Kitaigorodskii. *J. Geophys. Res.*, **69**, 5181–5190.
- Ropelewski, C. F., and P. D. Jones, 1987: An extension of the Tahiti–Darwin Southern Oscillation index. *Mon. Wea. Rev.*, **115**, 2161–2165.
- Semedo, A., Ø. Sætra, A. Rutgersson, K. Kahma, and H. Pettersson, 2009: Wave-induced wind in the marine boundary layer. *J. Atmos. Sci.*, **66**, 2256–2271.
- Simmons, A. J., S. M. Uppala, D. P. Dee, and S. Kobayashi, 2006: ERA-Interim: New ECMWF reanalysis products from 1989 onwards. *ECMWF Newsletter*, No. 110, ECMWF, Reading, United Kingdom, 25–35.
- , K. M. Willett, P. D. Jones, P. W. Thorne, and D. P. Dee, 2010: Low-frequency variations in surface atmospheric humidity, temperature, and precipitation: Inferences from reanalyses and monthly gridded observational data sets. *J. Geophys. Res.*, **115**, D01110, doi:10.1029/2009JD012442.
- Smith, S. D., and Coauthors, 1992: Sea surface wind stress and drag coefficients: The HEXOS results. *Bound.-Layer Meteor.*, **60**, 109–142.
- Snodgrass, F. E., G. W. Groves, K. F. Hasselmann, G. R. Miller, W. H. Munk, and W. M. Powers, 1966: Propagation of swell across the Pacific. *Philos. Trans. Roy. Soc. London*, **A259**, 431–497.
- Sterl, A., 2004: On the (in-)homogeneity of reanalysis products. *J. Climate*, **17**, 3866–3873.

- , and S. Caires, 2005: Climatology, variability and extrema of ocean waves: The Web-based KNMI/ERA-40 wave atlas. *Int. J. Climatol.*, **25**, 963–997, doi:10.1002/joc.1175.
- , G. J. Komen, and D. Cotton, 1998: 15 years of global wave hindcasts using ERA winds: Validating the reanalyzed winds and assessing the wave climate. *J. Geophys. Res.*, **103**, 5477–5492.
- Sullivan, P. P., J. B. Edson, T. Hristov, and J. C. McWilliams, 2008: Large-eddy simulations and observations of atmospheric marine boundary layers above nonequilibrium surface waves. *J. Atmos. Sci.*, **65**, 1225–1254.
- Trenberth, K. E., and J. W. Hurrell, 1994: Decadal atmosphere-ocean variations in the Pacific. *Climate Dyn.*, **9**, 303–319.
- Uppala, S. M., 1997: Observing system performance in ERA. ECMWF Re-Analysis Final Rep. Series 3, 261 pp.
- , and Coauthors, 2005: The ERA-40 Re-Analysis. *Quart. J. Roy. Meteor. Soc.*, **131**, 2961–3012.
- von Storch, H., and F. Zwiers, 1999: *Statistical Analysis in Climate Research*. Cambridge University Press, 494 pp.
- WAMDI Group, 1988: The WAM model—A third generation ocean wave prediction model. *J. Phys. Oceanogr.*, **18**, 1775–1810.
- Wang, X. L., and V. R. Swail, 2001: Changes of extreme wave heights in Northern Hemisphere oceans and related atmospheric circulation regimes. *J. Climate*, **14**, 2204–2221.
- WASA Group, 1998: Changing waves and storms in the northeast Atlantic? *Bull. Amer. Meteor. Soc.*, **79**, 741–760.
- WISE Group, 2007: Wave modelling—The state of the art. *Prog. Oceanogr.*, **75**, 603–674, doi:10.1016/j.pocean.2007.05.005.
- Young, I. R., 1999: Seasonal variability of the global ocean wind and wave climate. *Int. J. Climatol.*, **19**, 931–950.